In *Understanding Dynamics of Geographic Domains*, edited by K. Hornsby and M.Yuan,2008, CRC Press.

# 7 Relating Visual Changes in Images with Spatial Metrics

*Nina Lam, Guiyun Zhou, and Wenxue Ju*

## CONTENTS

Introduction ..... 115
Criteria for Selecting Spatial Metrics ..... 116
Methods ..... 119
Spatial Autocorrelation Statistic — Moran's I ..... 119
Image Characterization and Modeling System (ICAMS) ..... 119
Visual Change Detection Examples ..... 120
Camera Images ..... 120
Landsat-TM images ..... 125
Conclusions ..... 128
References ..... 129

## INTRODUCTION

Visualizing land cover and feature changes from time-series remote sensing images is the first and fundamental step in understanding the change dynamics of many geographic phenomena. In general, changes that are drastic and spatially concentrated can be discerned more easily, whereas small and gradual changes that scatter are very difficult to detect. Moreover, human visualization is not sufficient to detect changes continuously and rapidly. We need computation and measurement to support visualization and help identify where and what are the visual changes. Visual representation alone cannot satisfy analytical needs (Thomas and Cook 2005). Therefore, relating the change dynamics observed visually with quantitative measures that can be computed from the images is very much needed to enhance the visualization capability. These measures or metrics would enable automation and hence rapid and continuous monitoring, which is crucial to supporting timely decision-making and risk assessment especially during extreme events (e.g., terrorist attacks, hurricanes, forest fires, earthquakes, disease spread).

At the same time, we need better visualization methods to display the results from measurements so that the most important information can be visualized quickly and easily. This necessitates two considerations. First, when analyzing land use and

land cover changes derived from time-series remote sensing images, some changes may not be real, as they may be due to difference in cloud cover, misregistration of images, seasonal change, and other extraneous effects. The remote sensing community has widely recognized this problem and has developed various approaches to minimize these effects. We argue in this chapter that the use of spatial metrics on band-ratio images for change detection would help in reducing the extraneous effects and detecting real changes. The main notion is that the use of spatial metrics, in combination with original spectral information in band-ratio form, will increase land cover and feature classification accuracy, as well as have great potential for rapid change detection (Lam, forthcoming). Second, the visualization routine should be able to highlight the largest or most important changes automatically, so that it can be used as guidance for interpreters to focus on areas that need attention most. Such seemingly simple routines are not easily applied in commercial image processing packages. Specialized computer software will need to be developed to facilitate both measurement and visualization concurrently.

Although a huge literature on change detection using remotely sensed images exists, and new approaches continuously appear in the literature, we are still far from being able to automate the change detection process. The high variability of ground conditions as manifested in individual and time-series imagery, as well as many other sources of uncertainty including the scale issues (Lam et al. 2004; McMaster and Usery 2004), make the process very difficult to generalize and automate. The search for useful approaches and methods for characterizing and modeling landscape dynamics, especially rapid land cover identification and change detection, remains a major research challenge in these fields (Bian and Walsh 2002).

The purpose of this chapter is to introduce the use of spatial metrics as an approach to detecting the change dynamics from time-series images and to link visualization and measurement in a seamless manner. The ultimate goal is to automate the change-detection process through close coupling of measurement and visualization. This chapter will first discuss the criteria for selecting appropriate spatial metrics for rapid change detection, since there are lots of spatial and textural indices in various literature, and not all of them are applicable. We will then introduce the use of classical Moran's $I$ spatial autocorrelation statistic, a spatial index that meets all the criteria, in change detection. Two examples illustrating the approach to linking visual changes with spatial metrics are demonstrated, one using digital camera images and the other using Landsat-TM images of New Orleans. The prospect and problems of using spatial metrics for change dynamic analysis are then evaluated.

## CRITERIA FOR SELECTING SPATIAL METRICS

These are numerous spatial or textural measures in the literature. Lam (forthcoming) outlined some of the commonly used spatial metrics, as well as the criteria for selecting a spatial metric for rapid change detection. For example, some measures are founded on vigorous statistical theory and mathematical derivation (e.g., fractals, wavelets, spatial autocorrelation), while others are based on geometric measurements with unknown statistical properties and theoretical minimum or maximum (e.g., edge density) (Haralick 1979; Haralick et al. 1973; Lam et al. 1998). Some metrics

measure one aspect of the landscape (e.g., landscape composition), while others quantify another (e.g., landscape configuration) (McGarigal and Marks 1995). There are also attempts to classify various spatial measures. Baskent and Jordan (1995) classified landscape indices as areal, linear, or topological. Yet another classification of spatial and textural measures is based on whether the measures are applied directly to the original matrix (first-order textural measures), or to matrices derived from the original matrix such as the gray-level co-occurrence matrix or wavelet decomposed images (second-order textural measures) (Jensen 2004). Hence, it is imperative to develop useful criteria to evaluate or classify these textural measures.

What is a good spatial or textural measure? Although there may be no definite answers until each measure is tested extensively for their discriminating and explanatory power, the following criteria will be used to evaluate and guide our understanding of these various measures (Lam, forthcoming). Ideally, a good spatial measure should have the following properties:

1. *The spatial measure should be conceptually simple and easy to calculate and visualize.* For example, statistical mean and standard deviation are concepts easily grasped by most researchers and their statistical properties are well known. Extension of these basic statistical measures in a spatial domain with some modifications may provide a useful first approximation towards an understanding of the land cover/land use pattern being studied. On the contrary, some measures may be conceptually simple but require additional steps for calculation, such as edge density, which may need an additional step or algorithm to find the edges.
2. *The spatial measure should have theoretical maximum and minimum.* For example, Moran's $I$, a most commonly used spatial autocorrelation statistic, has a range of ±1. A Moran's $I$ value of 1.0 indicates a maximum positive spatial autocorrelation, a –1.0 indicates a maximum negative spatial autocorrelation, and a value of 0.0 indicates a random pattern (Cliff and Ord 1973).
3. *The spatial measure should reflect clearly and intuitively the characteristics of the image pattern in a consistent manner.* For example, a lower fractal dimension value means a less spatially complex image, therefore given an image computed with a fractal dimension value of 2.3, we should be able to infer that this image is far less complex than an image computed with a fractal dimension value of 2.7, and a visual display of the two images should be able to reveal the difference (Lam 1990). Fractal dimension ($D$) also has the second property, where $D$ is expected to range from 2.0–3.0 for surfaces and 1.0–2.0 for lines (Mandelbrot 1982).
4. *The statistical properties of the spatial measure should be known to provide statistical confidence of the computed value.* For example, theoretically a Moran's $I$ value of 0.0 indicates a random pattern. If a pattern yields a computed value of 0.2, can we determine if this value is statistically the same or different from 0.0 to conclude that the pattern is random or not? Fortunately, the statistical properties of Moran's $I$ are relatively well known and hypothesis testing of whether a computed $I$ value is significant can be conducted. Under the assumption of randomization, the first and second

moments of the Moran's *I* value can be computed and the statistical significance of the value determined (Goodchild 1986). On the contrary, the statistical properties of fractal dimension are still not clear, even though it has well-defined theoretical minimum and maximum. Hence, it is difficult to judge, for example, if an image with a fractal dimension of 2.3 is significantly different from another image with a fractal dimension of 2.4. It is noted that the statistical properties of most spatial measures are very difficult to derive and therefore remain unclear; many researchers have resorted to the Monte Carlo approach to develop empirical probability functions for statistical hypothesis testing (e.g., Openshaw 1989).

5. *The spatial measure can be computed globally for the entire study area or locally for a local neighborhood.* For example, some landscape metrics are only applicable at either the patch, class, or landscape levels, instead of being applicable to all levels (McGarigal 2002), whereas Moran's *I* and fractals, as implemented in a software module called ICAMS (Image Characterization And Modeling System), can be applied both globally and locally to capture local change (Lam 2004; Emerson et al. 2005).
6. Finally, *the spatial measure should be applicable directly to both classified and unclassified images.* For example, the landscape metrics in FRAGSTATS were developed exclusively for categorical maps (O'Neill et al. 1988; McGarigal 2002), or in other words, classified images, though some of the metrics can be modified so that they can be applied to unclassified images. On the contrary, fractals, Moran's *I*, local variance (Woodcock and Strahler 1987), variogram, and lacunarity (all available in ICAMS) can be applied to both unclassified and classified images.

This last property is considered very important to automated land cover and land use classification and change detection for two reasons. First, if they can be applied directly to unclassified images, changes in the images can be detected prior to the tedious classification process. Only after the changes are determined to be significant, then it is necessary to identify or classify what the changes are. This is considered a more efficient approach, especially for continuous environmental monitoring. Second, since these spatial indices measure the spatial variations among pixels instead of comparing pixel by pixel, they are more likely to reflect dominant changes rather than spurious changes that might have resulted from using images taken in different time periods. If there are only small changes in land cover, it is expected that the spatial relationship will not alter and the spatial index values will remain the same. On the contrary, if there are significant land-cover changes, then it is expected that the spatial structure will be altered, and the spatial indices that are designed to measure the spatial structure should be able to capture these changes.

## METHODS

### Spatial Autocorrelation Statistic — Moran's I

Spatial autocorrelation statistics have been commonly used to measure the degree of clustering, randomness, or fragmentation of a spatial pattern. The two most common spatial autocorrelation measures for interval-ratio data are Moran's $I$ and Geary's $C$ (Cliff and Ord 1973). Moran's $I$ is generally preferred over Geary's $C$, because the values of the former are more intuitive (i.e., positive values for positive autocorrelation and vice versa). Moran's $I$ was also found to be generally more robust (Goodchild 1986). Moran's $I$ is calculated from the following formula:

$$I(d) = \frac{n \sum_i^n \sum_j^n w_{ij} z_i z_j}{w \sum_i^n z_i^2} \tag{7.1}$$

where $w_{ij}$ is the weight at distance $d$ so that $w_{ij} = 1$ if point $j$ is within distance $d$ from point $i$; otherwise, $w_{ij} = 0$; $z$'s are deviations from the mean for variable $y$, and $w$ is the sum of all the weights where $i \neq j$. Moran's $I$ varies from +1.0 for perfect positive correlation (a clumped pattern) to –1.0 for perfect negative correlation (a checkerboard pattern). A Moran's $I$ value of 0.0 would indicate a random pattern.

Moran's $I$ and Geary's $C$ were originally developed for measuring polygonal data (e.g., geographical regions) where the number of units or points measured ($n$) is often smaller. Only recently have these two measures been applied to raster data such as remotely sensed images, where the number of units being measured ($n \times n$) is much larger (Emerson et al. 1999; Lam et al. 2002). This could affect the utility of Moran's $I$ in characterizing image complexity. In a benchmark study using simulated fractal surfaces, Lam et al. (2002) found that for surfaces that have low fractal dimension (low complexity), Moran's $I$ was found to be ineffective and did not reflect accurately the complexity of the simulated surfaces. But for surfaces with high dimension (e.g., remotely sensed images), Moran's $I$ performed well and adequately reflected the spatial complexity of the surfaces, even though the range of Moran's $I$ values was small. However, a major advantage of Moran's $I$ is that, in addition to meeting all the criteria listed above, it is very stable computation-wide and with less ambiguity, and it can be applied with a small window size (Myint et al. 2004). Moran's $I$ and fractal dimension ($D$) have an inverse relationship, in which a spatial pattern with a high degree of fragmentation will have a low Moran's $I$ but a high fractal dimension (Lam et al. 2002).

### Image Characterization and Modeling System (ICAMS)

Both Moran's $I$ and Geary's $C$ have already been implemented in ICAMS, which was developed in the 1990s by the author and her collaborators (Lam et al. 1998 and 2002; Quattrochi et al. 1997). Other major indices have also been implemented, including fractals, wavelets, lacunarity, and variogram analysis. With ICAMS, these

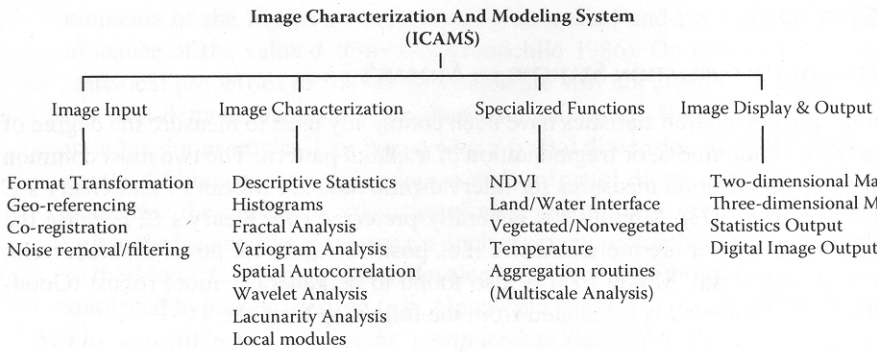


**FIGURE 7.1** Main functions of the Image Characterization And Modeling System (ICAMS).

indices can be computed globally (applied to the entire study area) or locally by varying the moving-window size.

ICAMS has four subsystems: image input, image output, image characterization, and specialized functions (Figure 7.1). ICAMS was developed with an objective of providing scientists with innovative spatial analytical tools to visualize, measure, and characterize landscape patterns so that environmental conditions or processes can be assessed and monitored more effectively. ICAMS was originally designed in the '90s as a module compatible with Arc/Info and Intergraph-MGE platforms. The software has since been re-programmed as a standalone module that can run on Windows without any need for extra software. ICAMS can be obtained via the authors. This research will utilize ICAMS for the computation of Moran's *I*, change detection, and input/output display. It is envisioned that ICAMS will serve as a platform for incorporating results from future related research, adding more useful routines or generalized models for automated change detection, and improving interactive capabilities between visualization and computation.

## VISUAL CHANGE DETECTION EXAMPLES

### Camera Images

Since the performance of using spatial indices for change detection is not well understood, we start with a set of simple images. Consider two photos taken from a digital camera at the backyard of a house in two time periods (Figure 7.2a and 7.2b). The first photo is without a person, and the second is with one, thus simulating a situation where there might be an intruder. The two images were taken with a time difference of less than one minute, and they were taken from a fixed photo stand, thus eliminating the possibility of errors from minor locational shifts. This controlled condition is rather unlikely for real satellite images, whereby the locations of two time-series images might not coincide exactly even after the geometric rectification process.

The RGB images (originally in JPEG format, then transformed to ERDAS/Imagine LAN format) were imported to ICAMS. Band 1 (red band) was selected for this experiment. The image size was 1536 × 2048 pixels. First, a difference image was created by subtracting the pre-image (without intruder) from the post-image (with

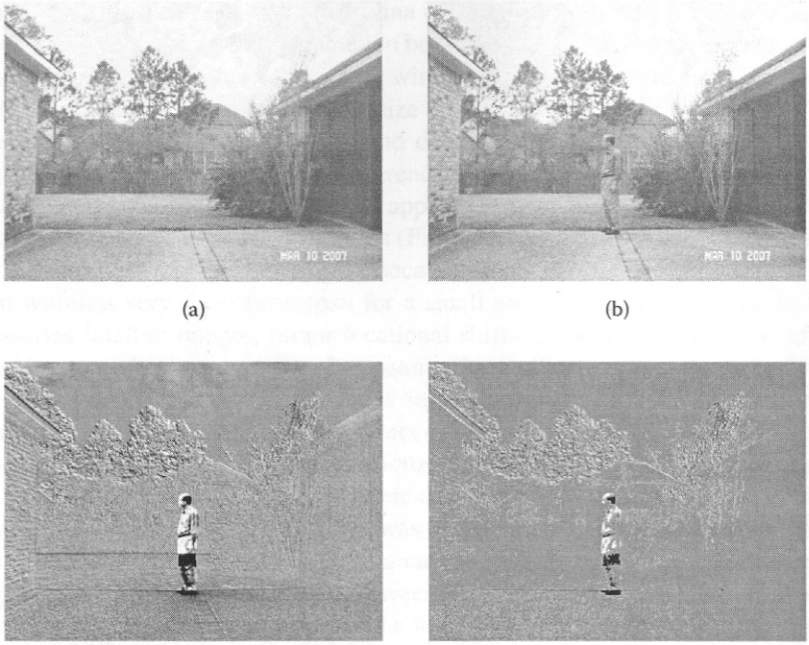


(a) (b)

(c) (d)

**FIGURE 7.2** Digital camera images displayed using the red band (band 1); (a) without suspect; (b) with suspect; (c) difference image (with-without) displayed in a continuous mode; (d) difference image displayed using 3 class intervals based on standard deviation unit of 2. The brightest and darkest pixels in this image indicate the highest positive and negative changes (>±2 s.d.), whereas the gray pixels are pixels that have values within ±2 s.d.

intruder) directly without any transformation. Figure 7.2c displays the difference image between the two time periods using a continuous mode (with a two-standard deviation stretch). To enhance visualization of the largest changes, ICAMS can map the difference image by dividing into classes using the standard deviation as class intervals, however. The purpose of this type of mapping is to pinpoint the largest changes in both positive and negative directions. Figure 7.2d was mapped using input parameters of 3 classes and standard deviation of 2. In other words, the first interval, which has the darkest shade, contains the largest negative difference, with pixel values below –2 standard deviations. The second class, which is in gray shade, is for pixels that have difference values falling between ±2 standard deviations. The third class, which is the brightest, is for pixels that have difference values >2 standard deviations. Using this mapping method, the brightest and the darkest pixels in the image are the pixels that have the largest positive and negative changes; hence logically attention should be paid to these areas first. This visualization method is simple and flexible, and should guide the user in finding the most "important" changes within a short amount of time. Another visualization option that is also available in ICAMS is to map the pixels that have both the largest positive and negative changes

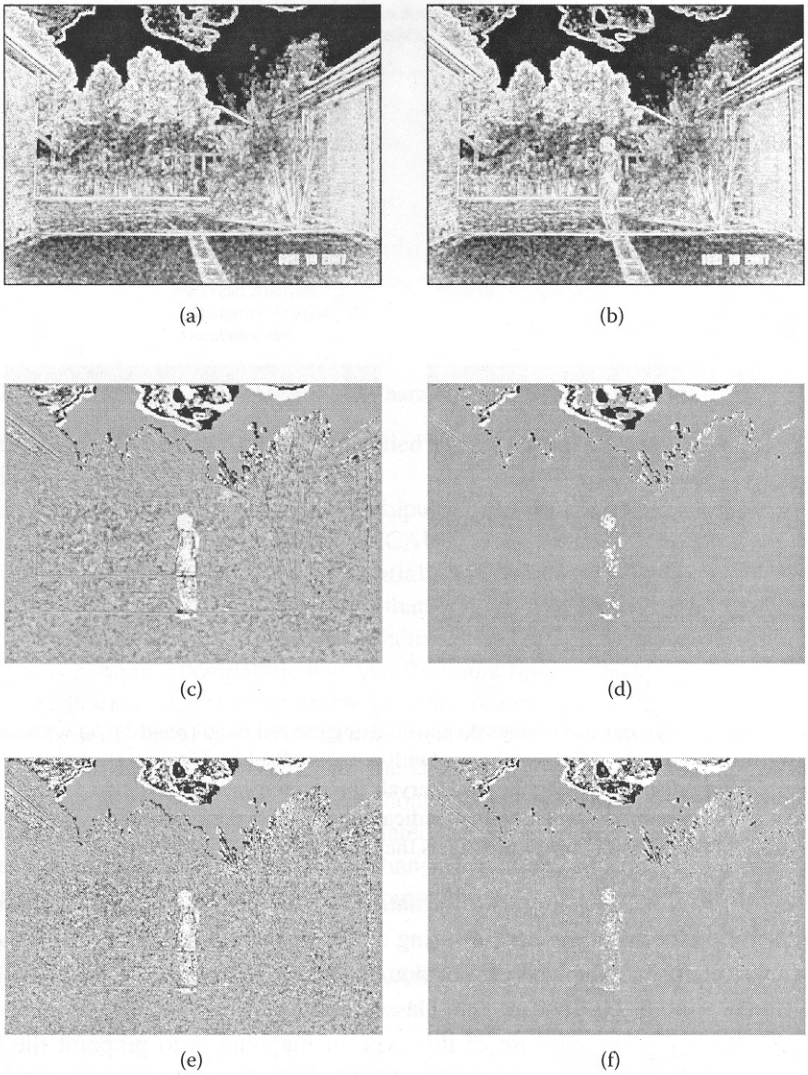


**FIGURE 7.3** (a) and (b) Moran's *I*-transformed camera images using the red band and moving window of 17 × 17 pixels, without and with suspect, respectively; (c) and (d) difference image (with-without) of 17 × 17 window, displayed in continuous and discrete modes; (c) and (d) difference image of 9 × 9 window, displayed in continuous and discrete class modes.

using the brightest shade; this is used when the direction of changes (positive or negative) is assumed to be equal in terms of attention to be received.

The two images were transformed by calculating Moran's *I* using two moving-window sizes: 17 × 17 and 9 × 9 pixels. Difference images (Figure 7.3) were then created and displayed in both continuous and discrete modes using the same procedure as in Figure 7.2. The 17 × 17 window was chosen because a previous study by Kulkarni (2004), in which Landsat-TM images were used to study the impacts of

Hurricane Hugo along the South Carolina coast, found that this window size (corresponding to 510 m by 510 m) seemed to be the best in capturing the characteristics of natural land cover features. The $9 \times 9$ window size was arbitrarily chosen to demonstrate the effects of moving-window size on the change detection process.

An examination of the brightest and darkest pixels in the original difference image (Figure 7.2c) shows that the difference image clearly revealed the location of the intruder. Minor spectral differences appeared in other parts of the image, which were classified and shown as gray pixels (Figure 7.2d). The difference image shown here is relatively free of noise, largely because the time-series camera images were taken within a very short time span for a small area using a fixed stand. In most time-series satellite images, minor locational shifts as well as atmospheric effects in the images often occur, even after geometric rectification and atmospheric correction. This will result in more noises in the difference image than the current example, making it more difficult to detect changes by using the spectral difference alone. A preliminary analysis using photos that were taken without a fixed stand (not shown here) indicated that there were a lot of noises in the simple spectral difference image, and the intruder object was no longer as clear as this current difference image, because of other differences caused by minor locational shifting of the images. The minor misregistration between the two photos when taken without a fixed stand was found to contribute to the largest but unimportant changes, in addition to the real change where the intruder stood.

The Moran's $I$ transformed images are difficult to interpret by themselves, which is expected, as they are not original images (Figure 7.3a and 7.3b). In general, the brighter the shade, the higher the Moran's $I$ value, implying higher positive spatial autocorrelation and hence a smoother surface. On the contrary, the darker the shade, the lower is the spatial autocorrelation value (negative values), hence a more rugged surface. Edges and lines become more prominent and are easily observed in these texture-transformed images.

The transformed difference image (Figure 7.3c and 7.3d) shows that, as expected, the largest difference occurred in the intruder's location, as well as along the edges between the sky and the trees. However, large differences in Moran's $I$ also occurred in the sky area, which is rather unexpected. An examination of the two transformed images found that the large differences occurred because some part of the sky area in the second image had very little variations but yielded high Moran's $I$ values because of the relatively smooth surfaces within the window (e.g., for row = 65, column = 1507, $I = 0.7919$); whereas in the first image they were completely flat (same spectral reflectance value), leading to Moran's $I$ values close to 0. In fact, the latter case resulted in a zero variance value that subsequently led to the computationally undefined problem. To avoid this computational problem, we replaced the zero variance with a very small value (0.00001), which then resulted in a Moran's $I$ value close to 0. This unexpected result is inconsistent with the theoretical explanation of Moran's $I$, where a value of close to 0 indicates a random surface rather than a flat surface. As far as the authors know, this special condition (a flat surface) and inconsistency in Moran's $I$ interpretation has seldom been reported in the literature, and a detailed analysis of the behavior of Moran's $I$ is necessary but is beyond the scope of this paper.

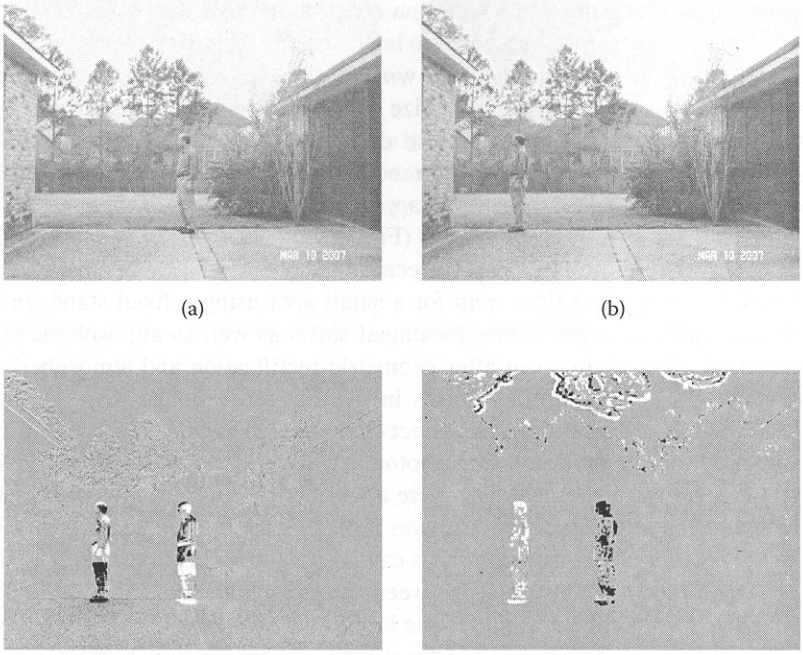


**FIGURE 7.4** (a) Original location of the intruder ($T_2$); (b) second location of the intruder ($T_3$); (c) and (d) difference image ($T_3$-$T_2$) displayed in continuous and discrete modes.

In terms of the effect of moving window size, when a smaller window size is applied to compute the texture, more details are revealed. The 9 × 9 transformed difference image (Figure 7.3e and 7.3f) shows the general trend as in the 17 × 17 transformed difference image but with more details. Based on visual comparison, it seems that for the current camera images, a 17 × 17 window is sufficient to reflect the changes. Hence it is used to demonstrate the next step.

To demonstrate the dynamics of changes, an additional photo depicting a change of the intruder location was taken to simulate a sequence of events. Figure 7.4a and 7.4b show the second ($T_2$) and the third ($T_3$) images. The spectral difference image between the third and the second images is shown in Figure 7.4c, and the Moran's *I* transformed difference image (using 17 × 17 windows) is shown in Figure 7.4d; both are displayed using the discrete class mode. Both images indicate clearly the location of the changes due to the movement of the intruder. This example shows that with additional images in a time sequence, more information can be revealed and the path of movement can be constructed.

These experiments using simple but real camera images show that misregistration and feature edges add difficulty in distinguishing real changes. The simple spectral difference image performs well because the camera images were taken from a fixed stand, thus eliminating most of the noises that were found in images taken without a fixed stand (images not shown). For textural transformed images such as Moran's *I*, the edge problem is more prominent. It is possible that in future research

an edge filter can be developed and applied to remove these effects, so that the search for real changes can be more focused. This example also demonstrates the importance of visualization, especially how the algorithm can be made to determine what to visualize.

## Landsat-TM images

We demonstrate in this example the use of spatial autocorrelation statistics for detecting and measuring changes from real satellite images. Two Landsat-TM images of New Orleans before and after Hurricane Katrina were used. Hurricane Katrina hit New Orleans on August 29, 2005. Two Landsat-TM images, dated November 7, 2004, and September 7, 2005, were obtained from the U.S. Geological Survey/National Wetlands Research Center at Louisiana State University (LSU). Although not acquired exactly on the same anniversary dates, these two images were the best available for change detection. Both images have already been registered and geometrically rectified with a pixel resolution of 28.5 m prior to this study.

For this study, a subset of 512 × 512 pixels was created at the same location from each image. Each subset was then converted into a ratio image, in this case a normalized difference vegetation index (NDVI) image. The use of ratio instead of individual spectral bands will help minimize the errors that might arise from comparing time-series images, such as difference in cloud cover, atmospheric effects, sun angles, and/or topographic effects. NDVI is a ratio between infrared and red bands, and is computed by:

$$NDVI = (Infrared - Red)/(Infrared + Red) \tag{7.2}$$

NDVI values range between ± 1.0. The index has been commonly used to delineate broad land cover classes such as vegetated versus nonvegetated areas, and water versus land. In general, clouds, snow, water, moist soil, and bright nonvegetated surfaces have NDVI values less than zero; rock and dry bare soils have values close to zero; and positive NDVI values generally indicate vegetated areas. In ICAMS, a value of -0.1 was set as the default threshold value to delineate water (< -0.1) and land (≥ –0.1). Similarly, a value of 0.25 was set as default value to delineate nonvegetated and vegetated boundaries. It is noted that such default values provide a starting point only, and the user will need to vary the threshold values to visualize and evaluate in order to find the values that best delineate the boundaries. Also, a fixed value may not work well in an urban setting like the present example.

Figure 7.5 displays the NDVI image subsets. The subsets are mainly confined to the Orleans Parish, with a small part of the Lower Ninth Ward in St. Bernard Parish shown at the east edge of the image (east of the Industrial Canal breach). The northwest corner of the image is Lake Pontchartrain, where significant storm surge has destroyed properties around the Lake. The three levee breaches at Industrial Canal, the 17th Street Canal, and the London Avenue Canal are also marked in the figure (Figure 7.5b). The NDVI difference image (post-pre) clearly shows the flooded areas of New Orleans, nine days after Katrina (Figure 7.5c). When displayed in discrete class mode (Figure 7.5d), largest negative changes in NDVI were found

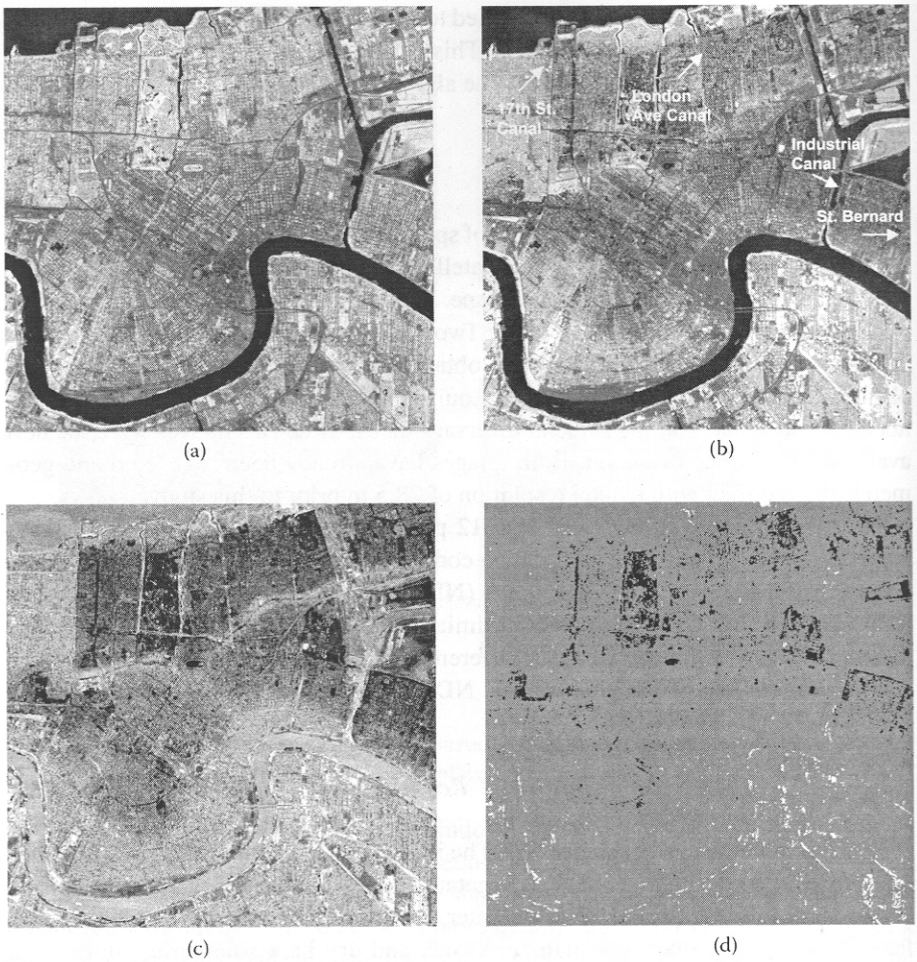


**FIGURE 7.5** (a) Pre-Katrina (Nov. 7, 2004) and (b) post-Katrina (Sept. 7, 2005) Landsat-TM NDVI images; (c) and (d) difference image displayed in continuous and discrete modes.

in the north-central part of the image, including areas such as the City Park (close to the London Ave. Canal breach).

Using ICAMS, we computed the local Moran's $I$ for each NDVI image using the same two window sizes, $9 \times 9$ and $17 \times 17$. Their difference images were then computed and displayed in both continuous and discrete modes (Figure 7.6). Table 7.1 lists the summary statistics of all the images. In general, the pre-Katrina NDVI image has more variation (coefficient of variation, CV = 0.34) than the post-Katrina NDVI image (CV = 0.23), due to a reduction of spectral variation because of the massive flooding. When the images are transformed, there is basically no difference in their coefficients of variation. Furthermore, when comparing the transformed images according to window size, larger moving-window size tends to create a smoother textural surface (higher mean $I$ values) with higher nonspatial variation

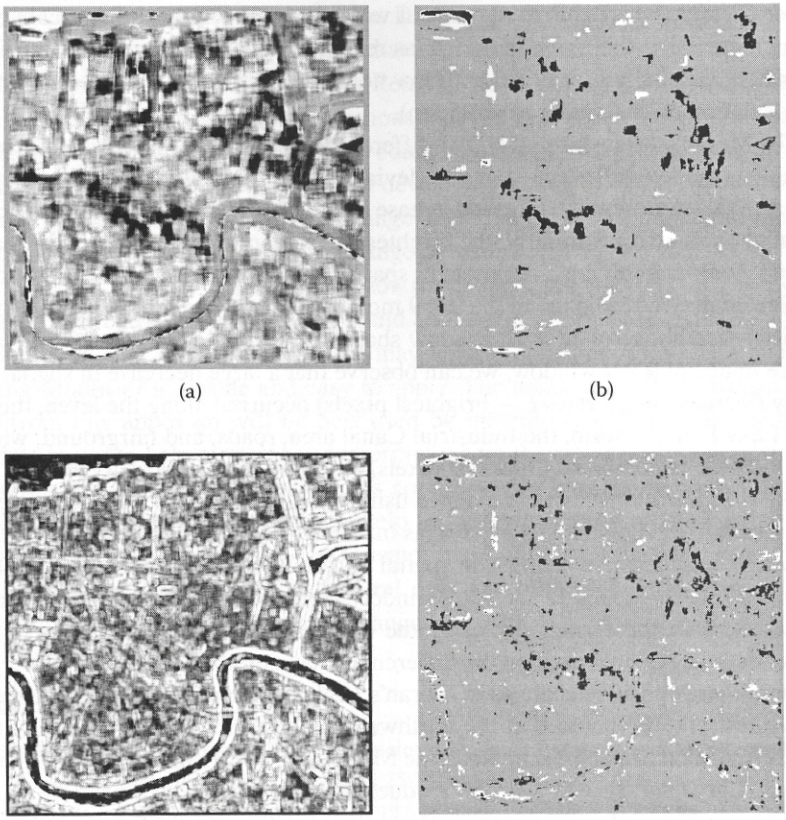


**FIGURE 7.6** (a) and (b) Difference images from Moran's *I* transformed pre- and post-images using moving windows of 17 × 17 pixels, and displayed in continuous and discrete modes; (c) and (d) difference image of 9 × 9 pixels and displayed in continuous and discrete modes.

**TABLE 7.1**
**Summary Statistics of Pixel Values in Pre- and Post-Katrina NDVI Images**

| | NDVI (scaled: 0-255) | | | Moran's *I* –Transformed (9 × 9) | | | Moran's *I* –Transformed (17 × 17) | | |
|---|---|---|---|---|---|---|---|---|---|
| | Pre | Post | Diff. | Pre | Post | Diff. | Pre | Post | Diff. |
| Min | 3.00 | 5.00 | 6.00 | –0.24 | –0.24 | –0.68 | –0.01 | –0.03 | –0.67 |
| Max | 255.00 | 255.00 | 255.00 | 0.94 | 0.94 | 0.71 | 0.97 | 0.97 | 0.66 |
| Mean | 130.21 | 148.15 | 148.68 | 0.54 | 0.53 | 0.01 | 0.64 | 0.64 | –0.00 |
| SD | 43.84 | 33.82 | 20.98 | 0.17 | 0.17 | 0.12 | 0.15 | 0.15 | 0.09 |
| CV | 0.34 | 0.23 | 0.14 | 0.18 | 0.18 | 12.00 | 0.23 | 0.23 | 9.00 |

* SD – standard deviation; CV – coefficient of variation (= SD/mean); Difference image = (post-pre).

(higher CV values). This is in agreement with the observation made in Lam (1990) that high spatial variation in an image (as reflected by low Moran's *I* or high fractal dimension) is usually associated with low nonspatial variation (as reflected by standard deviation or coefficient of variation).

The Moran's *I* transformed NDVI difference images were first mapped using the continuous mode (with a two-standard deviation stretch) (Figure 7.5a and 7.5c). The darkest pixels represent the largest decrease in Moran's *I* value, implying an increase in spatial complexity. Similarly, the brightest pixels represent the largest increase in Moran's *I* value, implying a decrease in spatial complexity. As expected, the difference image derived from using the $9 \times 9$ moving-window has more details, whereas the difference image of $17 \times 17$ window shows the general trend. Based on the difference image of $9 \times 9$ window, we can observe that a large decrease in spatial complexity (increase in Moran's *I* — brightest pixels) occurred along the levee, the edge along Lake Pontchartrain, the Industrial Canal area, roads, and fairground, whereas large increase in complexity (darkest pixels) scattered in the Mid-City area.

The difference images were mapped using the discrete mode with parameters set as ±2 standard deviation and 3 classes (as in Figure 7.2). Using this method, the largest positive and negative changes in spatial complexity can be pinpointed. Both the difference images of $17 \times 17$ and $9 \times 9$ windows generated the same general locations of interest, with the former depicting the dominant trend and the latter showing smaller details. Again, based on the difference image of $9 \times 9$ window (Figure 7.6d), in general, large positive changes in Moran's *I* values (decrease in spatial complexity — brightest pixels) occurred at the northwest corner of the image (Lake Pontchartrain), 17th Canal Street breach, along the Mississippi River, and some spots south of the river. Large decrease of Moran's *I* value (increase in spatial complexity — darkest pixels) were found scattered throughout the Mid-City areas. The exact locations of these changes and their interpretations can be identified by overlaying other GIS layers such as the road maps, which is beyond the scope of this chapter.

In summary, this example shows that the textural approach can be useful in pinpointing the areas that need the most attention. With additional information layers, identification of the exact location of the changes and interpretation of why such changes occur can be made effectively. Additional real images in a time sequence will also be useful to improve the change detection ability and to increase our understanding of the land change dynamics after a major disaster. Other mapping methods (such as the regular density slicing method) could further be employed to enhance the mapping and visualization of these changes.

## CONCLUSIONS

Visualization of dynamic changes needs analytic methods and measurement to quantify and help understand the observed changes and their underlying processes. At the same time, the need to visualize efficiently and intelligently will help in pushing the development of useful methods for change detection. Although change detection is an active research area in many fields with many algorithms and approaches developed, we are still far from being able to automate these tasks. The high variability of ground conditions as manifested in individual as well as time-series images makes it

very difficult to generalize and automate. Despite the difficulty, automated methods that can narrow the search for changes that are significant and warrant attention are possible and will need to be developed. Relating visual changes with spatial metrics is an attempt toward this goal. We demonstrated in this paper how spatial metrics such as spatial autocorrelation statistics could be used in change detection, which is a first step towards the long-term goal of developing a suite of visual routines to support and facilitate rapid and reliable change detection for environmental monitoring and for further understanding of the change dynamics.

The results from the two examples show that using spatial metrics such as Moran's *I* computed directly from the images could add useful information. Although a special condition (flat surface) exists that may lead to spurious results, the approach of using Moran's *I* is simple and easy to apply. The areas of greatest changes identified from this approach will be best used by integrating information from other GIS data layers to help pinpoint and interpret where the changes are and what other environmental and social characteristics are associated with them. Algorithms that can remove the edge effects will also help in narrowing the search for meaningful changes. Future research is needed to experiment with more indices, explore how these indices are integrated with spectral data and other data layers, and develop algorithms to remove "meaningless" changes.

## REFERENCES

Baskent, E.Z. and G.A. Jordan. 1955. Characterizing spatial structure of forest landscapes. *Canadian Journal of Forest Research* 25:1830–49.

Bian, L. and S.J. Walsh. 2002. Characterizing and modeling landscape dynamics: An introduction. *Photogrammetric Engineering and Remote Sensing* 68(10):999–1000.

Cliff, A.D. and J.K. Ord. 1973. *Spatial Autocorrelation*. New York: Methuen.

Emerson, C.W., N.S.N. Lam, and D.A. Quattrochi. 1999. Multiscale fractal analysis of image texture and pattern. *Photogrammetric Engineering and Remote Sensing* 65(1):51–61.

Emerson, C.W., N.S.N. Lam, and D.A. Quattrochi. 2005. A comparison of local variance, fractal dimension, and Moran's I as aids to multispectral image classification. *International Journal of Remote Sensing* 26(8):1575–88.

Goodchild, M.F. 1986. Spatial Autocorrelation. *CATMOG* (Concepts and Techniques in Modern Geography), no. 47. Norwich, England: Geo Books.

Gopal. S. and C. Woodcock. 1996. Remote sensing of forest change using artificial neural networks. *IEEE Transactions on Geoscience and Remote Sensing* 34(2):398–404.

Haralick, R.M. 1979. Statistical and structural approaches to texture. *Proceedings of IEEE* 67(5):786–804.

Haralick, R.M., K. Shanmugan, and J. Dinstein. 1973. Textural features for image classification. *IEEE Transaction on Systems, Man, and Cybernetics* 3(6):610–21.

Jensen, J. 2004. *Introductory Digital Image Processing: A Remote Sensing Perspective*, 3rd ed. Upper Saddle River, NJ: Prentice Hall.

Kulkarni, A. 2004. Evaluation of the Impacts of Hurricane Hugo on the Land Cover of Francis Marion National Forest, South Carolina Using Remote Sensing. M.S. thesis, Louisiana State University, Baton Rouge, Louisiana.

Lam, N.S.N. 1990. Description and measurement of Landsat TM images using fractals. *Photogrammetric Engineering and Remote Sensing* 56(2):187–95.

Lam, N.S.N. 2004. Fractals and scale in environmental assessment and monitoring. In *Scale and Geographic Inquiry: Nature, Society, and Method*, ed. E. Sheppard and R. McMaster, 23–40. Oxford, UK: Blackwell.

Lam, N.S.N. Forthcoming. Methodologies for mapping land cover/land use and its change. In *Advances in Land Remote Sensing: System, Modeling, Inversion and Application*, ed. S. Liang. New York: Springer.

Lam, N.S.N, H.L. Qiu, D.A. Quattrochi, and C.W. Emerson. 2002. An evaluation of fractal methods for characterizing image complexity. *Cartography and Geographic Information Science* 29(1):25–25.

Lam, N.S.N., D.A. Quattrochi, H.L. Qiu, and W. Zhao. 1998. Environmental assessment and monitoring with image characterization and modeling system using multiscale remote sensing data. *Applied Geographic Studies* 2(2):77–93.

Lam, N.S.N., C. Catts, D.A. Quattrochi, D. Brown, and R. McMaster. 2004. Scale. In *A Research Agenda for Geographic Information Science*, ed. R. McMaster, L. Usery, 93–128. Boca Raton: CRC Press.

Mandelbrot, B. 1982. *The Fractal Geometry of Nature*. New York: Freeman.

McGarigal, K. 2002. Landscape pattern metrics. In *Encyclopedia of Environmentrics*, Vol. 2, ed. A. H. El-Shaarawi, W. W. Piegorsch, 1135–42. Sussex, UK: Wiley.

McGarigal, K. and B.J. Marks. 1995. FRAGSTATS: Spatial pattern analysis program for quantifying landscape structure. *USDA Forest Service General Technical Report* PNW-351, Portland, OR.

McMaster, R. and L. Usery, eds. 2004. *A Research Agenda for Geographic Information Science*. Boca Raton: CRC Press.

Myint, S., N.S.N. Lam, and J. Tyler. 2004. Wavelet for urban spatial feature discrimination: comparisons with fractals, spatial autocorrelation, and spatial co-occurrence approaches. *Photogrammetric Engineering and Remote Sensing* 70(8):803–12.

O'Neill, R.V., J.R. Krummel, R.H. Gardner, G. Sugihara, B. Jackson, D.L. DeAngelis, B.T. Milne, M.G. Turner, B. Zygmunt, S.W. Christensen, V.H. Dale, and R.L. Graham. 1988. Indices of landscape pattern. *Landscape Ecology* 1:153–62.

O'Neill, R.V., A.R. Johnson, and A.W. King. 1989. A hierarchical framework for the analysis of scale. *Landscape Ecology* 7(1):55–61.

Openshaw, S. 1989. Automating the search for cancer clusters. *Professional Statistician* 8:7–8.

Quattrochi, D.A, N.S.N. Lam, H.L. Qiu, and W. Zhao. 1997. Image characterization and modeling system (ICAMS): A geographic information system for the characterization and modeling of multiscale remote sensing data. In *Scaling in Remote Sensing and GIS*, ed. D. Quattrochi and M. Goodchild, 295–307. Boca Raton: CRC/Lewis Publishers.

Thomas, J.J. and K.A. Cook. 2005. *Illuminating the Path: The Research and Development Agenda for Visual Analytics*. Los Alamitos, CA: IEEE Computer Society.

Woodcock, C.E. and A.H. Strahler. 1987. The factor of scale in remote sensing. *Remote Sensing of Environment* 21:311–32.